Journal of Power Sources 257 (2014) 1–11

Contents lists available at ScienceDirect

Journal of Power Sources

journal homepage: www.elsevier.com/locate/jpowsour

A lumped-parameter electro-thermal model for cylindrical batteries

Xinfan Lin [a,*], Hector E. Perez [a], Shankar Mohan [b], Jason B. Siegel [a], Anna G. Stefanopoulou [a], Yi Ding [c], Matthew P. Castanier [c]

[a] Department of Mechanical Engineering, University of Michigan, Ann Arbor, MI 48109, USA
[b] Department of Electrical Engineering and Computer Science, University of Michigan, Ann Arbor, MI 48109, USA
[c] U.S. Army Tank Automotive Research, Development, and Engineering Center (TARDEC), Warren, MI 48397, USA

HIGHLIGHTS

- An electro-thermal model capturing battery SOC, voltage, skin and core temperature.
- A convenient parameterization method identifying the two sub-models separately.
- Validation of the identified model with electrochemical impedance spectroscopy.
- Experimental validation with cycles covering 20–100% SOC, 5–38 °C, and max C-rate 20C.

ARTICLE INFO

Article history:
Received 3 September 2013
Received in revised form
9 January 2014
Accepted 9 January 2014
Available online 31 January 2014

Keywords:
Lithium ion batteries
Electro-thermal model
Parameterization
Core temperature
State of charge

ABSTRACT

Combining several existing lumped-parameter models, this paper presents an electro-thermal model for cylindrical batteries. The model consists of two sub-models, an equivalent-circuit electrical model and a two-state thermal model which are coupled through heat generation and temperature dependence of the electrical parameters. The computationally efficient 5-state model captures the state of charge (SOC), terminal voltage, surface temperature and the often neglected core temperature of a battery for wide range of operating conditions. The proposed parameterization scheme allows separate identification of the electric and thermal sub-models, greatly reducing the complexity of the parameterization process. The methodology is applied to a $LiFePO_4$/graphite battery. Comparison with the electrochemical impedance spectroscopy data clarifies the frequency range of the model fidelity. The model is further validated with two drive-cycle tests, covering SOC range 25%–100%, temperature 5 °C–38 °C, and maximum C-rate of 22C.

© 2014 Elsevier B.V. All rights reserved.

1. Introduction

Vehicle electrification, including application of hybrid electric vehicles (HEV), plug-in electric vehicles (PHEV) and battery electric vehicles (BEV), has been considered as a promising solution to the upcoming energy and environmental issues. Among all types of batteries, lithium ion batteries are nowadays widely used for automotive applications due to their advantages in energy/power density, charge efficiency among others. Correct estimation of the electrical and thermal dynamics of batteries is critical for safe and efficient operation. Model based observers have been widely considered for such purpose, where electrical models are used to estimate the state of charge (SOC) and voltage [1–3], and thermal models are applied for temperature monitoring [4–7].

The criteria for judging the quality of a control-oriented model include model fidelity, computational efficiency and ease of parameterization. Existing electrical models vary in complexity and fidelity. In some applications, where the applied current is small and simple, a coulomb counting-based OCV-R model is sufficient [8]. Such model consists of an SOC-dependent open circuit voltage (OCV) and an ohmic resistance. More complicated models, such as partial differential equation (PDE)-based electrochemical models [9–11], have also been used to capture the electrochemical processes during battery operation, giving more accurate voltage estimation over a wide range of current inputs. However, these models are computationally intensive and difficult to parameterize [12]. To balance complexity and fidelity, equivalent circuit models [1,13,14] are widely adopted in battery management systems (BMS),

* Corresponding author.
E-mail address: xflin@umich.edu (X. Lin).

0378-7753/$ – see front matter © 2014 Elsevier B.V. All rights reserved.
http://dx.doi.org/10.1016/j.jpowsour.2014.01.097

where a series of resistor-capacitor (R–C) pairs are used to capture the voltage dynamics.

For temperature estimation of the cylindrical battery, existing PDE-based thermal models can predict the detailed temperature distribution throughout the battery [10,15,16]. However, like the electrochemical models, these models are not easy to compute in real time and parameterize. Therefore, single-state models, where the thermal dynamics are represented by a bulk temperature [17,18], have been widely used due to their computational efficiency. Nevertheless, such approximation might lead to over-simplification since the temperature in the battery core can be much higher than in the surface [19]. Two-state thermal models capturing both the surface and the core temperatures have also been studied in Refs. [6,19–21]. Such models are capable of estimating the core temperature, and are efficient for control practice due to their limited number of states.

Electro-thermal models constructed by combining the electrical and thermal models introduced above have also been studied broadly. Some of these works are conducted with pure PDE-based approaches, such as [15,22], where an electrochemical model is coupled with a heat-equation based thermal model. Some apply lumped models to capture both the electrical and thermal dynamics, such as [23] (equivalent-circuit electrical model + single-state thermal model), and [4] (equivalent-circuit + lumped thermal model along the longitudinal direction). Others apply mixed approaches. For example, in Refs. [10,24], the electrical dynamics are modeled by an electrochemical model, and a single-state thermal model is used to capture the bulk temperature.

In this paper, a new control-oriented electro-thermal model is formulated by integrating an equivalent-circuit electrical model with a two-state thermal model. The thermal model captures the surface and core temperatures as the two states. Compared with the single-state model, this model provides higher fidelity with minimal increase in complexity, and it is more computationally efficient than the PDE-based models. Parameters of the electrical model are dependent on temperature, SOC and current direction. As a result, model parameterization can be computationally expensive and time consuming, requiring large dataset and advanced optimization methods, such as the genetic algorithm [1]. The parameterization strategy developed in this paper allows separate identification of electrical and thermal parameters in a straightforward way by isolating the dynamics of each sub-model. The electrical parameters are first identified under isothermal and SOC-invariant conditions for different temperatures, SOCs and current directions, similar to the method in Ref. [25]. The thermal model is then parameterized with a drive-cycle test using the heat generation calculated based on the current and voltage measurement and the open circuit voltage in the electrical model. The designed method has been applied to an A123 $LiFePO_4$/graphite battery. As an extension of [26], in this paper, frequency response of the modeled voltage dynamics is studied by comparing the model impedance with the electrochemical impedance spectroscopy (EIS) measurement. The identified electro-thermal model is also validated by two drive-cycle tests. Good model fidelity is achieved under high current, shown by a drive-cycle test with maximum current rate of 22C and temperature variation between 25 °C and 38 °C.

2. Coupled electro-thermal battery model

In this section, a coupled electro-thermal model is formulated for cylindrical batteries. The terminal voltage is captured by an equivalent circuit model, and a two-state thermal model is adopted to estimate the core and surface temperatures. The parameters of the electrical model depend on temperature, SOC and current direction, while the thermal parameters are treated as constant.

2.1. Electrical model

The schematic of an equivalent circuit model is shown in Fig. 1. Under a current I (positive for discharge), the terminal voltage V_T is modeled in three parts as

$$V_T = V_{OCV} - IR_s - \sum_{i=1}^{n} V_{RC,i}. \tag{1}$$

The first part is the open circuit voltage, V_{OCV}, which is usually a nonlinear function of SOC. The SOC is calculated by coulomb counting as

$$\frac{dSOC}{dt} = -\frac{1}{C_{bat}} I, \tag{2}$$

where C_{bat} is the battery capacity. The second part is the voltage drop over a series resistor R_s, accounting for the ohmic resistance. The last part is the voltage drop across a series of parallel R–C circuits, $V_{RC,i}$, which are used to approximate the voltage dynamics during transients. The dynamics of each R–C pair, $V_{RC,i}$, are described as

$$\frac{dV_{RC,i}}{dt} = -\frac{1}{R_i C_i} V_{RC,i} + \frac{1}{C_i} I, \tag{3}$$

where R_i and C_i are the equivalent resistance and capacitance. Typically, the values of R_i and C_i vary with SOC, current direction, and temperature which is captured by the thermal model to be introduced in Section 2.2. It will be shown in Section 3.1 that inclusion of more R–C pairs improves the model fidelity at the cost of complexity.

2.2. Two-state thermal model

By assuming longitudinal homogeneity, a two-state model [6,20], as shown in Fig. 2, is used to capture the lumped thermal dynamics of a cylindrical battery. Governing equations of T_c and T_s are [6,20],

$$\begin{aligned} C_c \frac{dT_c}{dt} &= Q + \frac{T_s - T_c}{R_c} \\ C_s \frac{dT_s}{dt} &= \frac{T_f - T_s}{R_u} - \frac{T_s - T_c}{R_c}. \end{aligned} \tag{4}$$

The heat generation Q in Eq. (4) is a byproduct of the chemical reactions taking place in the electrode assembly during battery operation. The value of Q is calculated based on the electrical model, as

$$Q = I(V_{OCV} - V_T), \tag{5}$$

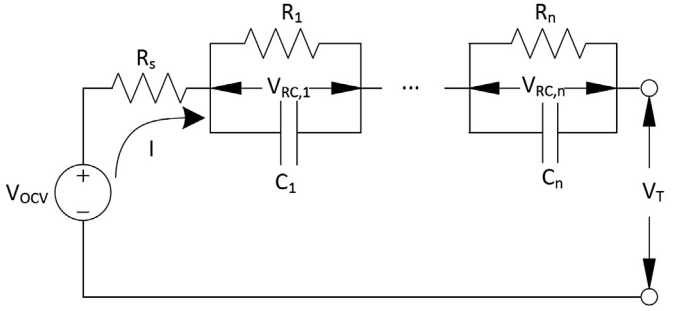

Fig. 1. Schematic of the equivalent circuit model.

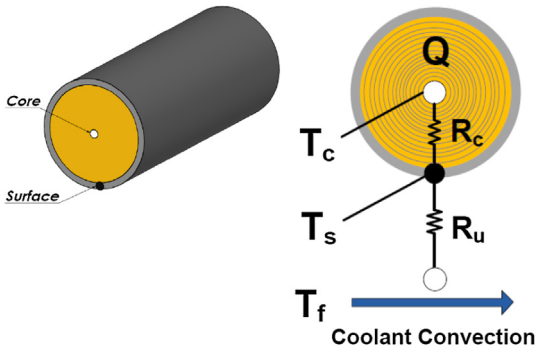

Fig. 2. Schematic of the two-state thermal model (adapted from Ref. [20]).

which includes the joule heating and energy dissipated in the electrode over-potentials [18]. For more accurate modeling of heat generation, reversible heat, such as entropic heat can be included [10,19]. A heat conduction resistance, R_c, is used to model the heat exchange between the core and the surface. Convective cooling through the battery surface is modeled by a convection resistance, R_u, between T_s and T_f. The value of R_u depends on the pack geometry, type of coolant and coolant flow rate. The rates-of-change of T_c and T_s are determined by the heat capacity of the core, C_c, and that of the casing, C_s.

2.3. Electro-thermal coupling

The electrical and the thermal sub-models interact with a two-way coupling, as shown in Fig. 3. First, the electrical model calculates the SOC and voltage of the battery based on the current I and the electrical parameters R_s, R_i and C_i. The difference between V_T and V_{OCV}, along with I, is used to determine the heat generation Q. The thermal model then calculates T_c and T_s based on Q and the ambient temperature T_f. The core temperature, T_c, which represents the temperature of the lumped electrode assembly, is used to determine the temperature-dependent parameters of the electrical model. The electro-thermal coupling complicates the parameterization of the model, which is usually conducted by fitting the parameters to match the measured outputs (V_T and T_s) from experiments. If the temperature is changing during the experiments, the temperature-dependent electrical parameters will also be varying, making them harder to identify. Experiments designed to excite the voltage dynamics without significantly changing the SOC or temperature are shown in Section 3. Therefore, the parameters will be constant (in each step of the experiments), and easy to identify.

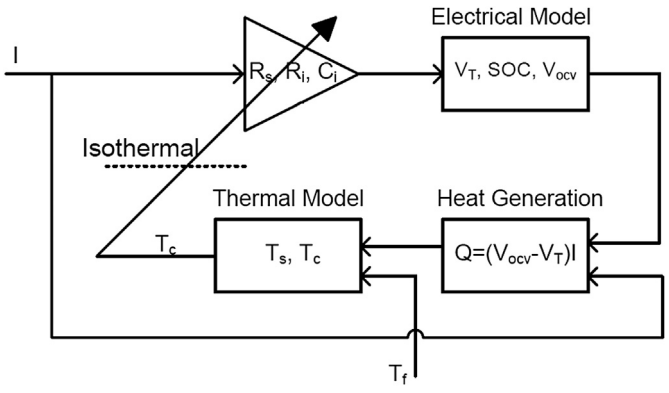

Fig. 3. Coupling between the electrical and the thermal models.

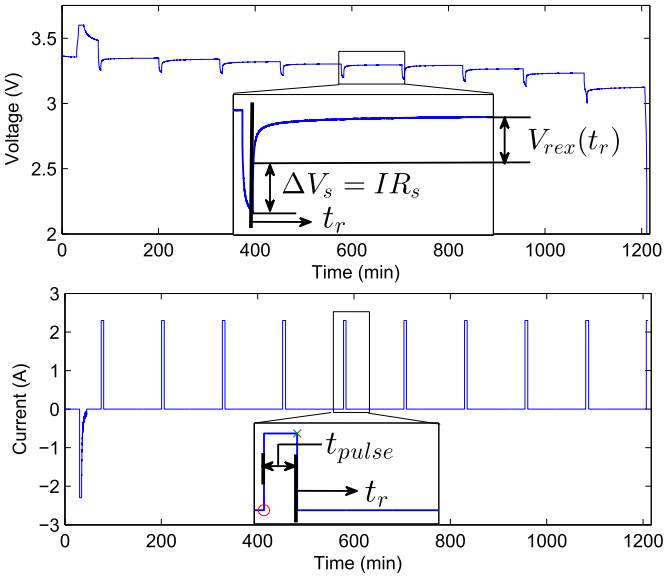

Fig. 4. Voltage and current profile during the discharging pulse test.

3. Model parameterization

In this section the methodology for parameterizing the electrical and thermal sub-models is described. First, the electrical parameters are identified based on a series of pulse-relaxation tests. Each test is performed under isothermal (and SOC-invariant) conditions. In this way, the electrical model is decoupled from the thermal model and can be identified independently. The tests are repeated under different SOCs, temperatures and current directions. The thermal model is then parameterized with the heat generation calculated based on the measured current, voltage and the identified open circuit voltage in the electrical model.

3.1. Parameterization of the electrical model

Parameterization of the electrical model involves identification of the open circuit voltage V_{OCV}, capacity C_{bat}, ohmic resistance R_s, and resistance and capacitance of the R–C pairs.

First, V_{OCV} and C_{bat} are determined by cycling the battery at a low current, e.g. C/20. The battery is charged with the constant current (CC) to the high voltage limit recommended by the manufacturer before switching to constant voltage (CV) charging until the current drops to the cut-off limit, e.g. C/50. The battery is then discharged to the low voltage limit with the same constant current used in charge. Since the voltage drop across the battery internal resistance is negligible under the low current, the difference between the charging and the discharging voltage is usually small. Therefore, either the charging or discharging voltage profile can be used as V_{OCV}. However, for some battery chemistries, e.g. $LiFePO_4$, the difference between the charging and discharging voltage can be much larger due to hysteresis [27,28]. In such case, the average of the charging and discharging voltage can be taken as the open circuit voltage, and the hysteresis in voltage may need to be modeled. The 100% SOC is defined at the end of the CV charge period, and 0% at the end of the discharge. The capacity C_{bat} is determined by the amount of charge between 0% and 100% SOCs.

The parameters of the equivalent circuits, including R_s, R_i and C_i, are identified based on the pulse-relaxation experiments. Tests are conducted in both discharge and charge current directions, and the discharge case is taken as an example for illustration. The battery is first charged to 100% SOC under the CC–CV protocol and then

relaxed for 2 h to reach electrical and thermal equilibrium. It is then discharged to 90% SOC with a current of 1 C (in around 6 min), which elevates the battery temperature only minimally. The current is then cut to relax the battery for 2 h. The voltage evolution during relaxation is recorded for identifying the R–C parameters. The procedures are repeated until the voltage reaches the low voltage limit. During the experiment, the battery is placed inside a thermal chamber, where the temperature is controlled at the desired set-point. To obtain the temperature dependency of the parameters, the test is performed at multiple temperatures. The voltage and current profiles during the discharge pulse test of a battery are plotted in Fig. 4. Voltage relaxation after each pulse, as shown in the inset of Fig. 4, is used to determine the parameters of the equivalent circuit at each SOC. It is noted that since both the temperature and SOC are constant during the relaxation, the parameters can be easily identified at fixed temperature. The ohmic resistance R_s is calculated by the initial voltage jump ΔV_s based on the Ohm's law,

$$R_s = \frac{\Delta V_s}{I}, \tag{6}$$

where I is the current applied during the pulse. The values of R_i's and C_i's are identified by using the relaxation voltage after the initial jump, $V_{rex}(t_r)$, shown in Fig. 4. The evolution of V_{rex} can be derived by solving Eq. (3), as

$$V_{rex}(t_r) = \sum_{i=1}^{n} IR_i\left(1 - e^{-\frac{t_p}{R_iC_i}}\right)\left(1 - e^{-\frac{t_r}{R_iC_i}}\right), \tag{7}$$

where t_p is the pulse duration before the relaxation. The resistance R_i and the capacitance C_i of each R–C pair are then fitted to minimize the least square error in voltage,

$$J = \min_{R_i,C_i} \sum_{k} \left(V_{rex}(k) - V_{rex,data}(k)\right)^2, \tag{8}$$

where $V_{rex,data}(k)$ is the measured relaxation voltage at each time instant k. The number of R–C pairs (n) can be determined based on the fitting results to be discussed later.

3.2. Parameterization of the thermal model

The parameters of the thermal model, including the conduction resistance R_c, convection resistance R_u, and heat capacities of the battery core and surface C_c and C_s, are identified based on the method developed in Refs. [6,29]. Considering the difficulty of measuring the core temperature T_c, parameterization is designed by only using the current I, surface temperature T_s and coolant flow temperature T_f, which can all be easily measured.

As the first step, a parametric model in the Laplace domain Refs. [30],

$$Z(s) = \theta^T \Phi(s) \tag{9}$$

needs to be derived. In Eq. (9), Z is referred to as the observation, θ is the parameter, and Φ is the regressor consisting of measured signals. For the thermal model in Eq. (4), the parametric model can be derived by performing Laplace transform to the governing equations and eliminating the unmeasured T_c by replacing with measured signals, as

$$\begin{aligned} s^2T_s(s) = {} & \frac{1}{C_cC_sR_c}Q(s) + \frac{1}{C_cC_sR_cR_u}\left(T_f(s) - T_s(s)\right) \\ & - \left(\frac{C_c + C_s}{C_cC_sR_c} + \frac{1}{C_sR_u}\right)sT_s(s). \end{aligned} \tag{10}$$

In the form of Eq. (9), we have

$$\begin{aligned} &\text{observation} : Z = s^2T_s(s) \\ &\text{regressors} : \Phi = \left[Q(s), \quad T_f(s) - T_s(s), \quad sT_s(s)\right]^T \\ &\text{parameters} : \theta = \left[\alpha, \quad \beta, \quad \gamma\right]^T, \end{aligned} \tag{11}$$

where the original physical parameters are now lumped into

$$\begin{aligned} &\alpha = \frac{1}{C_cC_sR_c}, \quad \beta = \frac{1}{C_cC_sR_cR_u}, \\ &\gamma = -\frac{C_cR_u + C_sR_u + C_cR_c}{C_cC_sR_cR_u}. \end{aligned} \tag{12}$$

The least squares algorithm is applied to identify θ [30] based on the parametric model,

$$\hat{\theta} = \left(\mathbf{\Phi^T\Phi}\right)^{-1}\mathbf{\Phi^T Z}, \tag{13}$$

where $\hat{\theta}$ is the estimate of θ. The parameter identification is performed in the time domain, and the matrices $\mathbf{Z}$ and $\mathbf{\Phi}$ consist of the signals Z and Φ at different time instant t_k during the experiment,

$$\begin{aligned} &\mathbf{Z} = \begin{bmatrix} \frac{z(t_1)}{m(t_1)} \\ \frac{z(t_2)}{m(t_2)} \\ \cdots \\ \frac{z(t_N)}{m(t_N)} \end{bmatrix}, \quad \mathbf{\Phi} = \begin{bmatrix} \frac{\phi^T(t_1)}{m(t_1)} \\ \frac{\phi^T(t_2)}{m(t_2)} \\ \cdots \\ \frac{\phi^T(t_N)}{m(t_N)} \end{bmatrix} \\ &m(t_k) = \sqrt{1 + \phi^T(t_k)\phi(t_k)}, \end{aligned} \tag{14}$$

where z and ϕ are the time-domain signals of Z and Φ, m is the normalization factor used to enhance the robustness of the algorithm, and N is the number of time instants. In Eq. (14), the needed time-domain signals z and ϕ include Q, T_s, T_f, and the first and second time derivatives of T_s (sT_s and s^2T_s in the time domain). The temperature T_s and T_f are measured, and Q is calculated based on Eq. (5). As for the time derivatives of T_s, in order to avoid differentiating the signals which is easily corrupted by noises, a second order filter

$$\frac{1}{\Lambda(s)} = \frac{1}{(s + \lambda_1)(s + \lambda_2)}, \tag{15}$$

needs to be used. The filtered parametric model will become

$$\begin{aligned} Z_f &= \theta^T\Phi_f \\ Z_f &= \frac{1}{\Lambda(s)}\left(s^2T_s\right) = \frac{s^2}{\Lambda(s)}T_s \\ \Phi_f &= \frac{1}{\Lambda(s)}\begin{bmatrix} Q & T_f - T_s & sT_s \end{bmatrix}^T \\ &= \begin{bmatrix} \frac{1}{\Lambda(s)}Q & \frac{1}{\Lambda(s)}\left(T_f - T_s\right) & \frac{s}{\Lambda(s)}T_s \end{bmatrix}^T. \end{aligned} \tag{16}$$

The time-domain signals of Z_f and Φ_f, z_f and φ_f will be used in Eq. (14) in place of z and ϕ, which are obtained by passing the measured/calculated signals through relevant filters, as shown in Fig. 5.

The 95% confidence interval of each identified parameter $\hat{\theta}_j$ can be calculated as [31]

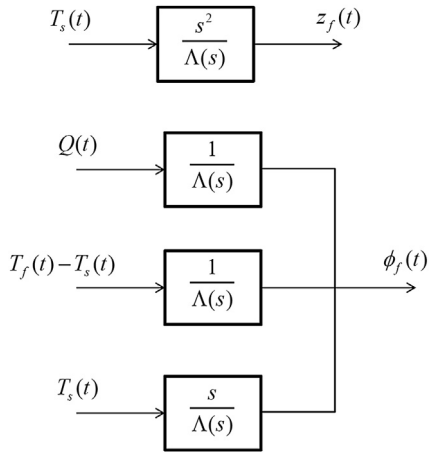

Fig. 5. Filtering of the signals used to identify the Thermal Model.

$$\widehat{\theta}_{\mathrm{j}} \pm 1.96\sqrt{\widehat{var}\left(\widehat{\theta}_{\mathrm{j}}\right)}. \tag{17}$$

The estimated variance of $\widehat{\theta}_j$, $\widehat{var}(\widehat{\theta}_{\mathrm{j}})$, is the diagonal element of the covariance matrix,

$$cov\left(\widehat{\theta}\right) = \left(\Phi^T\Phi\right)^{-1}\sigma^2, \tag{18}$$

where σ^2 is the variance of z_{f},

$$\sigma^2 = \frac{\sum_{\mathrm{k}}\left(z_{\mathrm{f}}(t_{\mathrm{k}}) - \widehat{\theta}^{\mathrm{T}}\phi_{\mathrm{f}}(t_{\mathrm{k}})\right)^2}{N}. \tag{19}$$

By using the above algorithm, the lumped parameters α, β and γ are identified. It is noted that only three of the four original parameters can be obtained based on α, β, and γ. Therefore, one of the parameters needs to be assumed in order to determine the other three. It is found that C_{s} can be easily calculated based on the specific heat capacity and dimensions of the casing. The estimates of R_{u}, R_{c} and C_{c} can then obtained by

$$\begin{aligned}\widehat{R}_{\mathrm{u}} &= \frac{\widehat{\alpha}}{\widehat{\beta}}, \quad \widehat{R}_{\mathrm{c}} = \frac{1}{\widehat{\alpha}C_{\mathrm{s}}\widehat{C}_{\mathrm{c}}},\\ \widehat{C}_{\mathrm{c}} &= -\frac{\widehat{\gamma}C_{\mathrm{s}}\widehat{R}_{\mathrm{u}} + \widehat{\alpha}C_{\mathrm{s}}^2\widehat{R}_{\mathrm{u}} + 1}{\widehat{\alpha}\widehat{R}_{\mathrm{u}}C_{\mathrm{s}}}.\end{aligned} \tag{20}$$

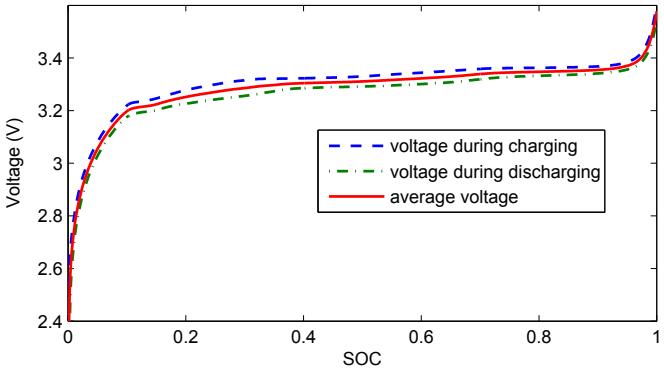

Fig. 7. Terminal voltage vs. SOC under C/20 charging/discharging tests.

4. Experiment setup

Experiments have been conducted on a 2.3 Ah *A*123 26650 $LiFePO_4$ battery to parameterize and validate the electro-thermal model. A Yokogawa GS-610 Source-Measure Unit was used for the tests to parameterize the electrical model. The C/20 CC–CV test was performed first to identify V_{OCV} and C_{bat}. The high and low voltage limits for this battery are 3.6 V and 2 V, and the cutoff current of CV is set at 50 mA. The unit was then programmed to run the pulse-relaxation tests to parameterize the R–C pairs. During the tests, the battery was cycled inside a Cincinnati Sub-Zero ZPHS16-3.5-SCT/AC thermal chamber, where the ambient temperature was controlled. The test is conducted between 5 °C and 45 °C at every 10 °C interval to obtain the temperature dependency of the parameters.

A drive-cycle, the scaled urban assault cycle (UAC) [32], which contains sufficient excitation [6], was used to parameterize the thermal model. The test was conducted with a Bitrode FTV1-200/50/2-60 cycler, which is capable of providing the power needed to simulate the drive-cycle. The battery was placed in a designed flow chamber with a fan regulating the air flow rate. The fan speed was fixed so that a constant convection resistance R_{u} would be identified. T-type thermocouples were installed on the battery surface to measure T_{s}, and inside the flow chamber to measure T_{f}. The measured T_{s} and T_{f} were used for model identification. In order to validate the identified thermal model, a thermocouple was also installed inside the battery to measure T_{c} [6]. The whole experiment setup is shown in Fig. 6.

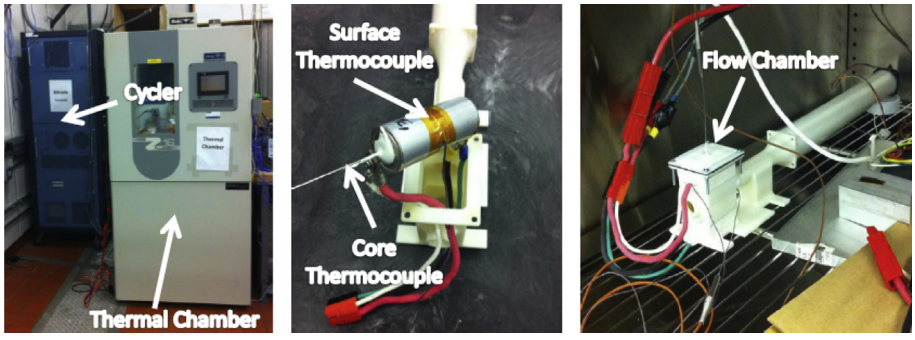

Fig. 6. Experiment setup.

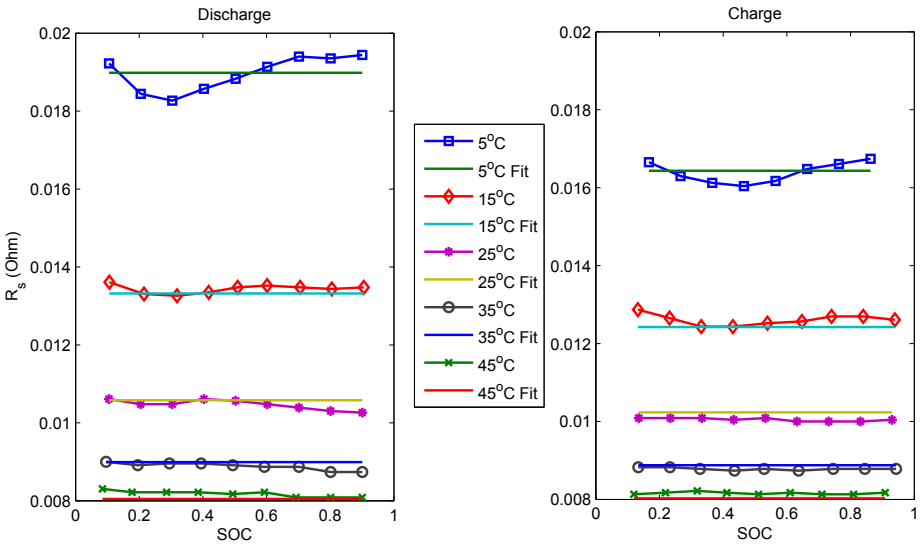

Fig. 8. R_s under different temperatures, SOCs and current directions.

5. Parameterization results

In this section, the parameters of the $LiFePO_4$/graphite battery identified based on the methodology discussed in Section 3 are demonstrated.

5.1. Identified parameters

The open circuit voltage V_{OCV} and capacity C_{bat} are first measured based on the C/20 cycling test. The measured terminal voltage is shown in Fig. 7. As mentioned, due to the hysteresis of the $LiFePO_4$ chemistry, a gap is observed between the charge and discharge voltage curves. The average of the two is taken as V_{OCV} and modeling of the hysteresis remains to be addressed. The actual battery capacity C_{bat} was measured at 2.1 Ah.

The series resistance R_s identified from the pulse-relaxation tests under different SOCs, temperatures and current directions is shown in Fig. 8. It can be seen that R_s has a minimal dependence on SOC over the tested range (10%–90% SOC), moderate dependence on current direction, and strong dependence on temperature. The value of R_s decreases as the temperature rises, dropping by more than 50% from 19.1 mΩ at 5 °C to 8.2 $m\Omega$ at 45 °C under discharge. This trend can be explained by the more active reaction kinetics at higher temperature. An Arrhenius-like function,

$$R_{s,l} = R_{s,0,l} \exp\left(\frac{T_{refRs,l}}{T_m - T_{shiftRs,l}}\right), \tag{21}$$

is used to fit the temperature dependency of R_s, where $l = c$ for charge, and $l = d$ for discharge.

To parameterize the rest of the electrical model, the number of R–C pairs needs to be determined first. Equivalent circuits with single, double and triple R–C pairs have been fitted to the relaxation voltage in the pulse-relaxation test. Comparison of the fitting is shown in Fig. 9. It can be seen that the single R–C model yields large error especially during the first 500 s of relaxation, whereas the error of the double R–C model is much smaller over the entire period. The improvement from the double R–C to the triple R–C model is much smaller. The double R–C model is hence chosen for its advantage in computational efficiency. The identified parameters of the double R–C pairs are shown in Figs. 10–13.

For R_1 and R_2, it can be seen that, similar to R_s, their values decrease as the temperature increases due to the more active kinetics at elevated temperature. Nevertheless, compared with R_s, R_1 and R_2 exhibit more prominent dependence on SOC. Interestingly, such dependence is opposite for charge and discharge. The charge resistance increases significantly in the high SOC range (80%–100%), whereas the discharge resistance is higher at SOCs near 0%. The observed SOC dependency is in accordance with those in Refs. [25], where the parameters identified at SOCs closer to 0% and 100% are available. A second order polynomial is used to fit the SOC-dependency of R_1 and R_2, and an Arrhenius-like function for temperature dependency,

$$R_{i,l} = (R_{0,i,l} + a_{1,i,l}SOC + a_{2,i,l}SOC^2)\cdot\exp\left(\frac{T_{refR,i,l}}{T_m - T_{shiftR,i,l}}\right),$$
$$i = \begin{cases} 1, \text{ for } R_1 \\ 2, \text{ for } R_2 \end{cases}, \quad l = \begin{cases} c, \text{ for charge} \\ d, \text{ for discharge} \end{cases}, \tag{22}$$

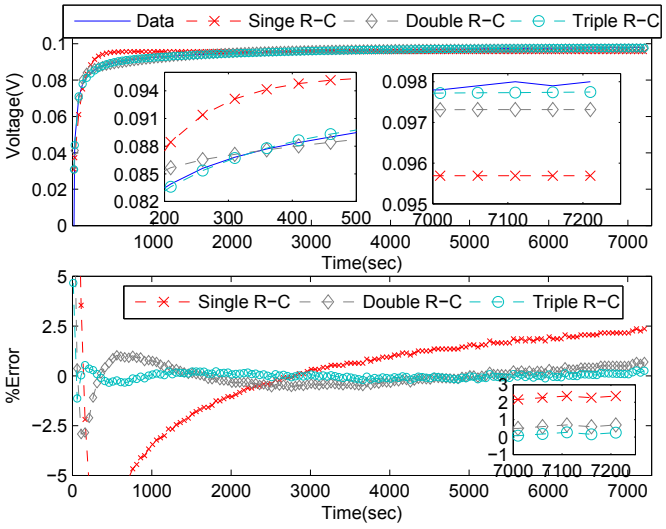

Fig. 9. Fitting of the relaxation voltage.

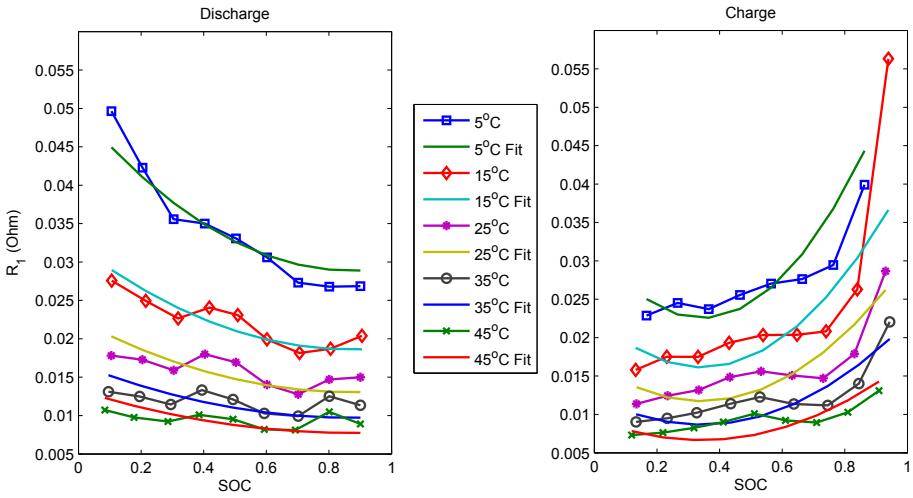

Fig. 10. R_1 under different temperatures, SOCs and current directions.

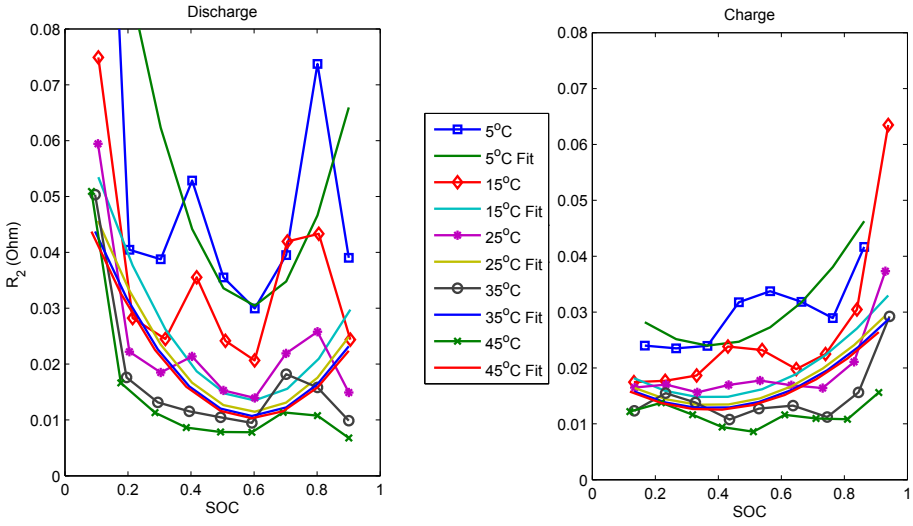

Fig. 11. R_2 under different temperatures, SOCs and current directions.

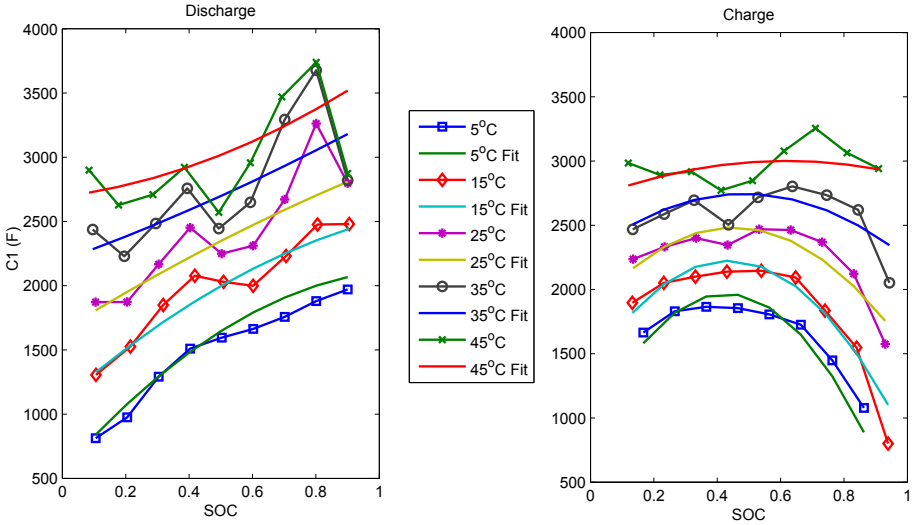

Fig. 12. C_1 under different temperatures, SOCs and current directions.

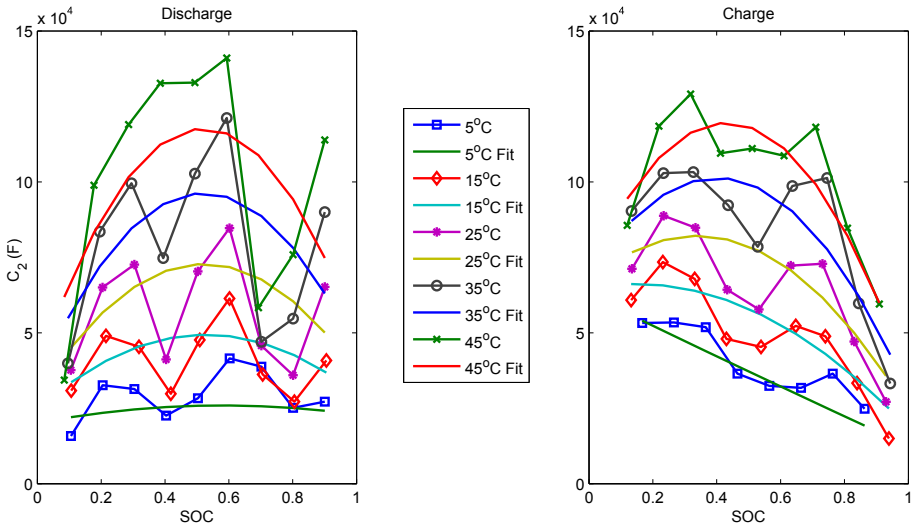

Fig. 13. C_2 under different temperatures, SOCs and current directions.

where $R_{0,i,l}$, $a_{1,i,l}$, and $a_{2,i,l}$ are the fitted parameters for the SOC dependency, and $T_{\mathrm{refR},i,l}$ and $T_{\mathrm{shiftR},i,l}$ are for the temperature dependency. The identified capacitances C_1 and C_2, plotted in Figs. 12 and 13, also show notable dependence on temperature and SOC. As opposed to the resistance, both capacitance values increase with temperature. For the SOC dependence, C_1 shows a nearly monotonically increasing trend from low to high SOC under discharge, while its values under charge are relatively constant in the low and middle SOC range but see a sharp decrease in the high SOC end. The relationship between C_2 and SOC is more complicated, as double peaks are observed. The values of C_1 and C_2 are each fitted by a quadratic function of SOC affine with temperature,

$$C_{i,l} = C_{0,i,l} + c_{1,i,l}(\mathrm{SOC}) + c_{2,i,l}(SOC)^2 + \left(c_{3,i,l} + c_{4,i,l}\left(\mathrm{SOC}\right) + c_{5,i,l}(\mathrm{SOC})^2\right)T_{\mathrm{m}},$$
$$i = \begin{cases} 1, & \text{for } R_1 \\ 2, & \text{for } R_2 \end{cases}, l = \begin{cases} \mathrm{c}, & \text{charge} \\ \mathrm{d}, & \text{discharge} \end{cases}. \tag{23}$$

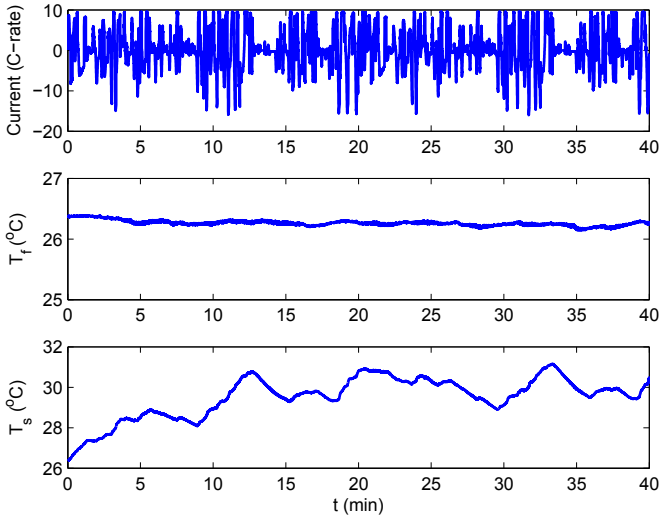

Fig. 14. Measured current, battery surface and flow temperatures under UAC.

The thermal model is parameterized by using data from the UAC drive-cycle test. The measured current I, coolant flow temperature T_{f}, and battery surface temperature T_{s} are shown in Fig. 14. The current I and measured V are used to calculate the heat generation along with the parameterized open circuit voltage based on Eq. (5). The pre-calculated C_{s} and identified C_{c}, R_{c} and R_{u}, along with the 95% confidence interval, are listed in Table 1. The identified thermal parameters are very close to those in Refs. [6], where the heat generation is calculated by using a single lumped internal resistance R_{e}, as $Q = I^2R_{\mathrm{e}}$. This lumped R_{e} includes the heat dissipation through the series resistance R_{s} and the R–C pairs of the equivalent circuit model in this paper. As pointed out in Refs. [6], the value of R_{e} can be cycle-dependent, or even non-constant within a single cycle due to the variability of battery resistance on temperature, SOC and other factors. Consequently, if a single R_{e} is used, its value needs to be obtained by online identification as in Ref. [6]. The identified R_{e} under the UAC is 11.4 $m\Omega$, which is in-between the series resistance R_{s} and the total resistance $R_{\mathrm{s}} + R_1 + R_2$ identified in this paper.

6. Validation of the identified model

This section is devoted to validating the identified electro-thermal model. The model dynamics are first investigated by comparing the model impedance with EIS measurements. The errors in voltage and temperature estimation under two drive-cycle tests will also be evaluated.

6.1. Comparison of the modeled electrical impedance with EIS

The battery impedance, Z, is the relationship between the current I and the terminal voltage V_{T} as a function of the current frequency,

Table 1
Identified parameters of the thermal model.

	Value	95% Confidence interval
C_{s} (JK^{-1})	4.5	–
C_{c} (JK^{-1})	62.7	59.1–66.4
R_{c} (KW^{-1})	1.94	1.86–2.01
R_{u} (KW^{-1})	3.19	3.19–3.20

$$V_T(j\omega) = Z(j\omega)I(j\omega), \tag{24}$$

where j is the imaginary unit, and ω is the angular frequency. For the electrical model in Eqs. (1)–(3), the impedance at T_0 and SOC_0, can be obtained based on the transfer function from the current to the voltage, with the model linearized at T_0 and SOC_0. The transfer function, $Z(s)$, is derived by taking Laplace transformation of the linearized model, as

$$\begin{aligned} V_T(s) &= Z(s)I(s) \\ Z(s) &= -\frac{\alpha}{C_{bat}}\frac{1}{s} - R_s - \frac{1}{C_1\left(s+\frac{1}{R_1C_1}\right)} - \frac{1}{C_2\left(s+\frac{1}{R_2C_2}\right)}, \end{aligned} \tag{25}$$

where α is the slope of V_{OCV}, and all parameters are evaluated at T_0 and SOC_0. By taking $s = j\omega$, the impedance $Z(j\omega)$ is obtained. The Nyquist plot of the modeled Z, where the real part $RE(Z)$ is plotted against the imaginary part $IM(Z)$, at 25 °C and 80% SOC, is shown in Fig. 15 as an example. It can be seen that the modeled impedance consists of two arcs in the high and middle frequency ranges, corresponding to the dynamics of the two R–C pairs. The intersection with the real axis represents the series resistance R_s.

The actual battery impedance can be measured by EIS, [33,34], where the battery is excited by AC currents with different frequencies and the response of the voltage is recorded to calculate the impedance. EIS has been performed under the open circuit condition, with an Autolab PGSTAT302N potentiostat/galvanostat under 50 mA AC currents, sweeping frequency from 0.1 mHz to 5 kHz. The Nyquist plot of the measured impedance is shown in Fig. 15, and the magnitude and phase of the impedance at different frequencies is plotted in Fig. 16 to compare with the model. As seen from Fig. 15, the measured impedance is composed of three parts, a semicircle in the frequency range higher than 1 Hz, corresponding to the dynamics of the passive films at the solid/electrolyte interface (SEI), an arc in the frequency range 2 mHz–1 Hz, representing the dynamics of the charge-transfer resistance and the double layer capacitance, and a straight line below 2 mHz, related to the dynamics of lithium diffusion [33,35].

The modeled impedance is more accurate between 0.01 Hz and 100 Hz than in the higher and lower frequency ranges, according to Fig. 16. The obtained accuracy in impedance is comparable to that in Refs. [36] and [37], where similar electrical models are analyzed. EIS has also been conducted at other SOCs, such as 60% and 95%,

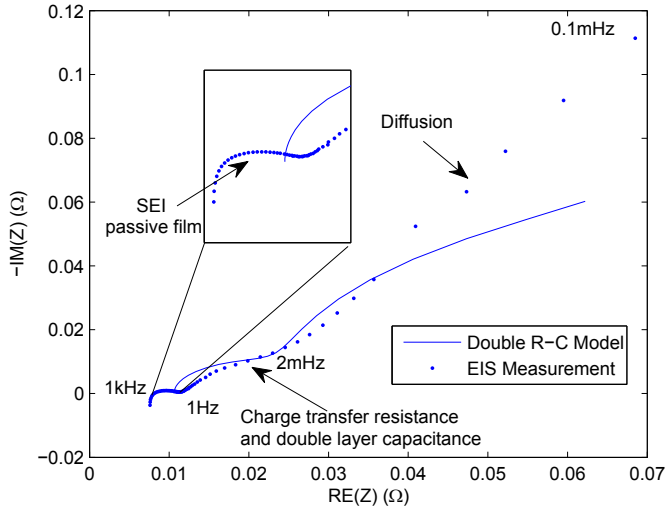

Fig. 15. Nyquist plot of the impedance: model vs. EIS measurement.

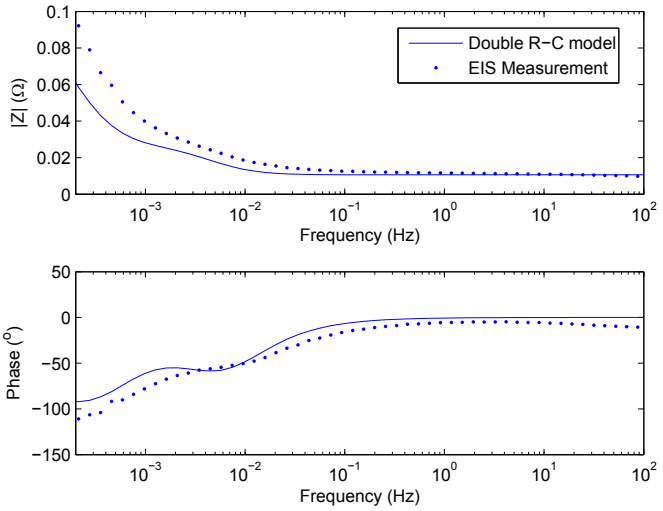

Fig. 16. Magnitude and phase of the impedance at different frequencies: model vs. EIS measurement.

revealing similar behavior. At the high frequency end, as shown in Fig. 15, the small semi-circle representing the dynamics of the SEI film is not modeled, as the right end of the semi-circle is captured as the series resistance R_s. The reason may be attributed to lack of fast voltage dynamics excited in the pulse-relaxation tests. In the low frequency range, the impedance is underestimated due to two possible reasons. As indicated by Eq. (25), the modeled impedance at low frequencies is related to the slope of V_{OCV}, α, as well as R_2 and C_2. For one thing, α may be inaccurate because of the flatness of V_{OCV} (as shown in Fig. 7) and exclusion of hysteresis in V_{OCV} modeling. For another, the pulse-relaxation voltage used to identified the R–C pairs is not very sensitive to the slow dynamics (R_2 and C_2), as compared to the fast dynamics (R_1 and C_1), which might compromise the accuracy of the identified R_2 and C_2. The full battery dynamics can be modeled more accurately based on the EIS data by using complex impedance components, such as constant phase elements (CPE) [33,34]. However, the modeling and parameterization procedure will be much more complicated, and the implementation of model in time domain is usually achieved by approximation with a significant number of R–C pairs [33]. The

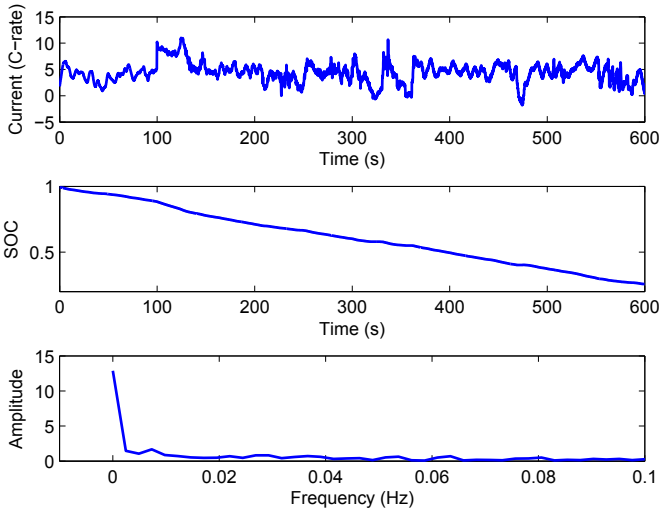

Fig. 17. Current profile and SOC variation of the charge-depleting cycle (top: current in time; middle:SOC; bottom: FFT of current).

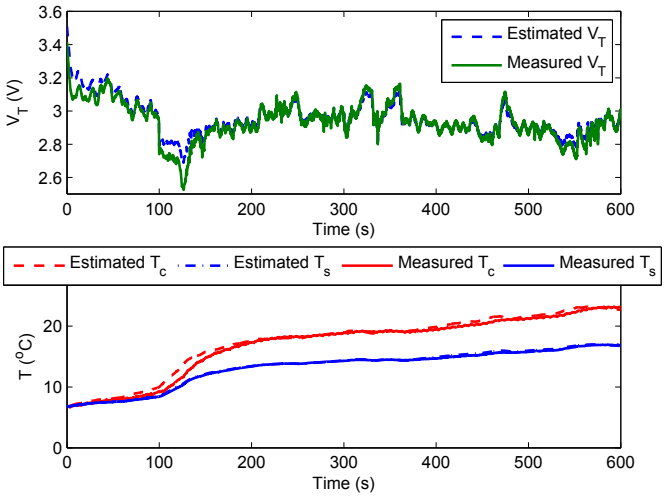

Fig. 18. Voltage and temperature estimation under the charge-depleting cycle.

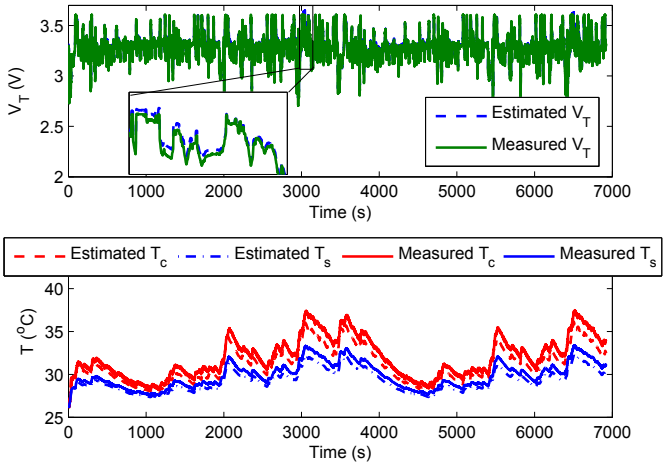

Fig. 20. Voltage and temperature estimation under the charge-sustaining cycle.

associated computational load may cause issues for onboard applications, especially when the number of cells are large.

6.2. Validation by drive-cycles

The model has also been validated by data from two drive-cycle tests. The current, SOC, and temperature variation of the validation cycles are plotted in Figs. 17–20. The first validation cycle is a charge-depleting (CD) cycle with maximum current around 10 *C* and average at 4 *C*. The battery SOC decreases from 100% to 25%, and the core temperature increases from 5 °*C* to 23 °*C* in approximately 10 min. The second validation cycle, shown in Figs. 19 and 20, is a more drastic and charge-sustaining (CS) cycle, where the maximum current is more than 20 *C*, and the average around 0.03 *C*. The resulting SOC varies between 30% and 53%, while the temperature fluctuates between 25 °C and 38 °C. The two cycles combined cover an SOC range from 25% to 100%, and a temperature range between 5 °C and 38 °C, which are roughly the ranges that the model parameters are identified in this paper. Fourier transformation has also been performed to demonstrate the frequency spectrum of the two cycles, as shown in Figs. 17 and 19. It can be seen that the CD cycle is slower and contains a peak at 0 Hz, which is the DC component corresponding to the mean charge-depleting rate. The dynamics of the CS cycle are faster and have more evenly distributed frequency content.

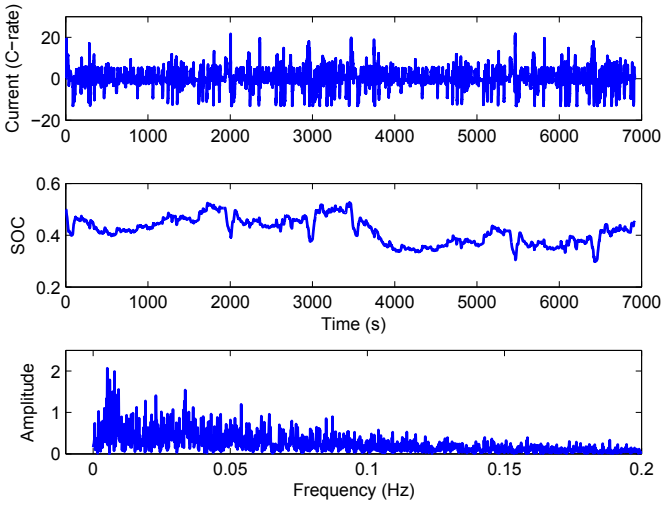

Fig. 19. Current profile and SOC variation of charge-sustaining cycle (top: current in time; middle:SOC; bottom: FFT of current).

The voltage and temperatures estimated by the parameterized model are plotted in Figs. 18 and 20 to compare with the measurements. The root mean square errors (RMSE) of the estimation by using parameters directly identified and based on fitted functions Eqs. (22) and (23) are listed in Table 2. It can be seen that the identified model shows good fidelity under the high-power charge-sustaining cycle, as the voltage RMSE is below 20 mV, and the temperature RMSE below 1°C. Larger voltage RMSE (45 mV) are observed in the charge-depleting cycle. The model performance is compared to that of similar electrical models under drive-cycle tests in Refs. [1,14]. In Ref. [1], an equivalent circuit electrical model with 2 RC pairs and 1 hysteresis state is parameterized and validated with a specific drive-cycle test. In Ref. [14], electrical models with 1–3 RC pairs and 1 hysteresis state are validated under the Dynamic Stress Test (DST) and Federal Urban Dynamic Schedule (FUDS) respectively. The specifications of the models and drive-cycles and the estimation errors are shown in Table 3. The voltage RMSEs of models in Ref. [14] are as small as 8 mV, partially due to the mild operating condition (small current rate and invariant temperature) besides the well identified model. The estimation error of the electro-thermal model in this paper under the CS cycle is close to that of the model in Ref. [1]. As for the CD cycle, there are several possible reasons for the larger voltage estimation error. First, hysteresis of the $LiFePO_4$ chemistry has not been included in the modeling. The nonlinear hysteresis dynamics in voltage are more prominent under unidirectional current than under charge-balance current profile. Second, it has been revealed by the EIS measurement that the battery voltage dynamics are not very well captured in the low frequency range (below 0.01 Hz), and the mismatch becomes larger as the frequency approaches 0 Hz (Figs. 15 and 16). The current profile of the CD cycle, whose frequency distribution has a high peak at 0 Hz corresponding to an

Table 2
Estimation errors when using parameters directly identified and parameters based on fitted functions.

RMSE	V_T (mV)	T_s (°C)	T_c (°C)
CD cycle (directly identified)	45.4	0.20	0.56
CD cycle (fitted function)	48.6	0.25	0.62
CS cycle (directly identified)	20.3	0.65	0.92
CS cycle (fitted function)	19.2	0.67	0.96

Table 3
Comparison of model performance under drive cycles.

	CS	CD	Cycle in Ref. [1]	DST [14]	FUDS [14]
Model description	2RC&thermal	2RC&thermal	2RC + hysteresis	1-3RC + hysteresis	1-3RC + hysteresis
Maximum C-rate	22	10	8.7	2	2
Average net C-rate	0.027	4	0.12	0.03	0.07
Temperature variation (°C)	25–38	5–23	−5–40	Constant	Constant
SOC variation	0.30–0.53	0.25–1	0.3–0.9	0.62–0.67	0.45–0.59
RMSE V_T (mV)	20.3	45.4	26	~8	~8
RMSE T_c (°C)	0.92	0.56	–	–	–
RMSE T_s (°C)	0.65	0.2	–	–	–

average net discharging rate of 4C, may contribute to the estimation error significantly. Specifically, as seen from Figs. 17 and 18, the largest voltage errors are observed between 100 s and 140 s, where the current is held around 8C for 40 s. This part alone results in 12 mV increase in the overall RMSE voltage error.

7. Conclusion

In this paper, an electro-thermal model for cylindrical batteries is proposed based on an equivalent-circuit electrical model and a two-state thermal model. The electrical and the thermal parts are coupled through heat generation and temperature dependency of the electrical parameters. The integrated 5-state model is computationally efficient for onboard applications and provides estimates of the critical battery states. The core temperature of cylindrical batteries, which is usually neglected by existing control-oriented models, is captured. As shown in Figs. 18 and 20, the core temperature can be significantly higher than the surface temperature, especially under high current. Accurate estimation of the core temperature can help reduce the risk of overheating. Additionally, since the parameters of the electrical model are temperature dependent, capturing the temperature close to the electrode assembly (core temperature) can also enhance the accuracy of voltage estimation. Such advantage is desirable especially under high current application where the temperature swing is large and fast.

The electrical sub-model is parameterized under isothermal conditions. Since the electrical and the thermal dynamics are decoupled, the parameters can be identified separately. Pulse-relaxation tests are used to parameterize the electrical model so that the SOC dependency of the parameters can be conveniently identified under SOC invariant conditions. The thermal model is then parameterized by using the heat generation calculated by the measured current, voltage and the electrical model. Such strategy greatly reduces the complexity of the parameterization.

Acknowledgment

The authors would like to thank the U.S. Army Tank Automotive Research, Development, and Engineering Center (TARDEC), and Automotive Research Center (ARC), a U.S. Army center of excellence in modeling and simulation of ground vehicles, for providing support including funding.

UNCLASSIFIED: Dist A. Approved for public release.

References

[1] Y. Hu, S. Yurkovich, Y. Guezennec, B.J. Yurkovich, J. Power Sources 196 (2011) 449–457.
[2] G.L. Plett, J. Power Sources 134 (2004) 262–276.
[3] S. Santhanagopalan, R.E. White, J. Power Sources 16 (2006) 1346–1355.
[4] K. Smith, G.-H. Kim, E. Darcy, A. Pesaran, Int. J. Energy Res. 34 (2010) 204–215.
[5] C. Mi, B. Li, D. Buck, N. Ota, in: Proceedings of IEEE Vehicle Power and Propulsion Conference, 2007.
[6] X. Lin, H. Perez, J. Siegel, A. Stefanopoulou, Y. Li, R.D. Anderson, Y. Ding, M. Castanier, IEEE Trans. Control Syst. Technol. 21 (2013) 1745–1755.
[7] M. Debert, G. Colin, G. Bloch, Y. Chamaillard, Control Eng. Pract. 21 (2013) 1035–1042.
[8] K. Kutluay, Y. Cadirci, Y.S. Ozkazanc, I. Cadirci, IEEE Trans. Industr. Electron. 52 (2005) 1315–1327.
[9] T.F. Fuller, M. Doyle, J. Newman, J. Electrochem. Soc. 141 (1994) 1–10.
[10] W.B. Gu, C.Y. Wang, J. Electrochem. Soc. 147 (2000) 2910–2922.
[11] C. Speltino, D. Domenico, G. Fiengo, A. Stefanopoulou, in: Proceedings of IEEE Conference on Decision and Control, 2000, pp. 3276–3281.
[12] J.C. Forman, S.J. Moura, J.L. Stein, H.K. Fathy, J. Power Sources 210 (2012) 263–275.
[13] M. Coleman, C.K. Lee, C. Zhu, W.G. Hurley, IEEE Trans. Industr. Electron. 54 (2007) 2550–2557.
[14] X. Hu, S. Li, H. Peng, J. Power Sources 198 (2012) 359–367.
[15] C. Wang, V. Srinivasan, J. Power Sources 110 (2002) 364–376.
[16] S.A. Hallaj, H. Maleki, J. Hong, J. Selman, J. Power Sources 83 (1999) 1–8.
[17] K. Smith, C. Wang, J. Power Sources 160 (2006) 662–673.
[18] D. Bernardi, E. Pawlikowski, J. Newman, J. Electrochem. Soc. 132 (1985) 5–12.
[19] C. Forgez, D. Do, G. Friedrich, M. Morcrette, C. Delacourt, J. Power Sources 195 (2010) 2961–2968.
[20] C. Park, A. Jaura, in: SAE 2003-01-2286.
[21] M. Muratori, N. Ma, M. Canova, Y. Guezennec, in: Proceedings of the ASME Dynamic Systems and Control Conference, 2010.
[22] L. Cai, R.E. White, J. Electrochem. Soc. 157 (2010) A1188–A1195.
[23] L. Gao, S. Liu, R. Dougal, IEEE Trans. Compon. Packag. Technol. 25 (2002) 495–505.
[24] W. Fang, O.J. Kwon, C.Y. Wang, Int. J. Energy Res. 34 (2010) 107–115.
[25] L. Lam, P. Bauer, E. Kelder, in: Proceedings of IEEE International Telecommunications Energy Conference, 2011.
[26] H.E. Perez, J.B. Siegel, X. Lin, A.G. Stefanopoulou, Y. Ding, M.P. Castanier, in: ASME Dynamic Systems and Control Conference (DSCC), 2012.
[27] M.A. Roscher, D.U. Sauer, J. Power Sources 196 (2011) 331–336.
[28] V. Srinivasan, J. Newman, Electrochem. Solid-State Lett. 9 (2006) A110–A114.
[29] X. Lin, H. Fu, H.E. Perez, J.B. Siegel, A.G. Stefanopoulou, Y. Ding, M.P. Castanier, Oil Gas. Sci. Technol. Rev. IFP Energ. Nouvelles, France 68 (2013) 165–178.
[30] P.A. Ioannou, J. Sun, Robust Adaptive Control, Prentice Hall, 1996.
[31] Encyclopedia of Statistics in Behavioral Science, Wiley, 2005.
[32] T. Lee, Y. Kim, A. Stefanopoulou, Z. Filipi, in: Proceedings of American Control Conference, 2011.
[33] T. Dong, A. Kirchev, F. Mattera, Y. Bultel, ECS Trans. 25 (2010) 131–138.
[34] J. Illig, M. Ender, T. Chrobak, J.P. Schmidt, D. Klotz, E. Ivers-Tiffe, J. Electrochem. Soc. 159 (2012) A952–A960.
[35] L. Liao, P. Zuo, Y. Ma, X. Chen, Y. An, Y. Gao, G. Yin, Electrochim. Acta 60 (2012) 269–273.
[36] D.V. Do, C. Forgez, K.E.K. Benkara, G. Friedrich, IEEE Trans. Veh. Technol. 58 (2009) 3930–3937.
[37] G. Prasad, C. Rahn, in: Proceedings of ASME Dynamic Systems and Control Conference, 2012.